# Time-Domain Analysis and Optimization of a Three-Phase Dual-Active-Bridge Converter With Variable Duty-Cycle Modulation

Gunnar Schulz and Jennifer Bauman, *Senior Member, IEEE*

***Abstract*—The duty-cycle control (DCC) modulation scheme for the three-phase dual-active-bridge (3p-DAB) dc–dc converter is a promising three degree-of-freedom modulation scheme which can extend the converter's soft-switching range and reduce conduction losses under partial loading and wide voltage variations. However, the prior suggested methods to implement DCC in 3p-DABs have drawbacks, such as requiring a multifrequency approximation and offline optimization process, or achieving less than optimal efficiency. To overcome these challenges, this article first proposes an optimal DCC modulation strategy (OMS) for the 3p-DAB based on a novel piecewise time-domain analysis (TDA) and optimization process that obtains the optimal control parameters for minimum rms phase current. Second, this article proposes a novel closed-form minimum current stress optimization (MCSO) DCC scheme based on the theoretical findings of the TDA optimization. The MCSO reduces the transformer phase currents and extends soft-switching operation under partial loading and wide voltage variations. Experimental results show that the proposed closed-form MCSO DCC scheme has virtually identical efficiency as the OMS, making this the first article to provide a closed-form DCC modulation scheme for a 3p-DAB that achieves efficiency results equivalent to a fully optimized offline scheme, but without the drawbacks of the offline optimization process.**

***Index Terms*—DC–DC converter, modulation, optimal control.**

## I. Introduction

With the increase in global attention toward electrified transportation, renewable power generation, and dc power distribution, the isolated bidirectional dc–dc converter (IBDC) is considered to be a key enabler in the development and integration of these technologies [1], [2], [3], [4]. The single-phase dual-active-bridge (1p-DAB) dc–dc converter is an attractive IBDC topology because of its high power density, galvanic isolation, and intrinsic soft-switching ability [5], [6]. The three-phase dual-active-bridge (3p-DAB) IBDC, however, offers some additional advantages compared to the 1p-DAB, such as increased power transfer capability, reduced device current stress, and smaller dc-link capacitance, which all contribute to an increase in power density [5]. Based on these advantages, this article focuses on the 3p-DAB topology.

The 3p-DAB is composed of two three-phase active bridges connected together by a high-frequency transformer with turns ratio *1:n* and leakage inductance *L*. For the conventional singe-phase-shift (SPS) modulation strategy, each switch in a leg has 50% complementary duty cycle and each leg is operated with a 120° phase-shift from another. By introducing a phase angle between the input and output bridges, power transfer can be controlled through the converter's leakage inductance. When a DAB converter is controlled using SPS modulation and is subject to partial loading with nonunity voltage gain *d*, its efficiency is reduced due to HSW and increased back power flow [7]. However, when IBDCs operate as auxiliary power modules in electrified vehicles or interface with renewable energy sources and storage devices, operation under partial loading and nonunity voltage gain is unavoidable. Therefore, to maintain efficient converter operation under a wider operating range, alternative modulation strategies must be implemented.

For the 1p-DAB, there exist many alternative modulation strategies that improve the performance of the converter under partial loading and nonunity voltage gain. By increasing the degrees of freedom in the control by introducing inner phase-shift angles, the dual-phase-shift [7], extended-phase-shift [8], and triple-phase-shift (TPS) [9] modulation strategies can be implemented to help mitigate back power flow and extend the soft-switching range of the converter. The TPS modulation strategy, having three degrees of freedom, can achieve globally optimized control parameters for minimum current stress (MCS), minimum rms current, minimum power loss, or maximum ZVS range [10]. However, these alternative modulation schemes cannot be directly applied to the 3p-DAB because of the 120° phase-shift that exists between phase legs.

Numerous modulation strategies have also been suggested to improve the performance of the 3p-DAB. In [11], parallel phase operation (PPO) of a 3p-DAB is proposed which operates the 3p-DAB as a 1p-DAB. This strategy improves the efficiency in the low and medium power range by leveraging optimal modulation strategies of the 1p-DAB; however, the paralleled phases cause increased dc-link ripple current and switching device stresses which negate the advantages of using a 3p-DAB.

Manuscript received 16 February 2023; revised 15 May 2023, 29 June 2023, and 27 July 2023; accepted 22 August 2023. Date of publication 1 September 2023; date of current version 23 October 2023. This work was supported in part by the Natural Sciences and Engineering Research Council of Canada under Discovery grant. Recommended for publication by Associate Editor A. Safaee. *(Corresponding author: Jennifer Bauman.)*

The authors are with the Department of Electrical and Computer Engineering, McMaster University, Hamilton, ON L8S 4L8, Canada (e-mail: schulg1@mcmaster.ca; jennifer.bauman@mcmaster.ca).

Color versions of one or more figures in this article are available at https://doi.org/10.1109/TPEL.2023.3311314.

Digital Object Identifier 10.1109/TPEL.2023.3311314

In [12], an asymmetrical phase-shift (APS) modulation scheme is proposed for the 3p-DAB to achieve minimum rms current by introducing variable phase-shifts between all phase-legs in the converter. While this strategy improves the efficiency compared to SPS modulation, the transformer phase currents are unbalanced, meaning different switches carry difference current levels, leading to uneven losses and the potential need to oversize switches. Moreover, the rms phase current is not minimized for each phase but rather the average rms phase current across all phases is minimized. In addition, in some power ranges, including the high-power range, the APS modulation scheme operates the 3p-DAB as a 1p-DAB, which again negates the advantages of using a 3p-DAB.

To add more flexibility to the 3p-DAB control and leverage the advantages of the three-phase topology, the duty cycles of the input and output bridges ($D_1$, $D_2$) and phase-shift ($D_{ps}$) can be modulated appropriately [13], [14], [15], [16], [17], [18], [19]. In [13], an optimal simultaneous PWM control strategy is proposed which applies the same variable duty cycle ($D_c$) to both active bridges to minimize the current stress. Although this control aims to minimize the peak current, it does not necessarily extend the soft-switching range, and since this control only employs two degrees of freedom ($D_c$, $D_{ps}$), there is no guarantee that the current stress is globally minimized.

Allowing a different duty cycle on the input and output bridges, as well as the phase-shift, gives three degrees of freedom, commonly called duty-cycle control (DCC). DCC for the 3p-DAB is analogous to TPS modulation for the 1p-DAB and therefore globally optimized modulation strategies can be obtained. The 3p-DAB modulation strategies proposed in [5] and [13] can be considered as special cases of DCC.

In [14], a DCC strategy is proposed for the 3p-DAB with the goal of optimizing control parameters to minimize the converter's rms phase current. The optimization process occurs offline, and the results are read from a look-up table (LUT) during converter operation. The 3p-DAB is modeled using the multifrequency approximation method, resulting in expressions of average output power and transformer rms currents that contain infinite series. To reduce the model's nonlinearity and computational burden, the infinite series must be truncated, which negatively affects the model accuracy, especially at light loads and nonunity voltage gain. In addition, only a simplified block diagram of the novel optimization algorithm used to obtain the optimal parameters is provided in [14], which hinders its practical implementation. Furthermore, the multifrequency approximation analysis in [14] is complicated and neglects to analyze the 3p-DAB boost operation, which is essential for many applications.

In [15], a phasor analysis approach is used in the proposed hybrid modulation scheme, which combines SPS and a novel zero-vector modulation scheme to target maximum 3p-DAB efficiency under wide voltage and power variations. The proposed modulation improves the efficiency of the converter compared to SPS during low-to-medium power and wide voltage gains; however, the modulation parameters ($D_1$, $D_2$, and $D_{ps}$) must be computed offline using a detailed loss model of the 3p-DAB which depends highly on component parameters that are sometimes difficult to determine, such as the high-frequency transformer Steinmetz parameters and switch parasitic capacitances. In addition to the detailed loss model, an offline optimization process is required, and the resulting parameters are implemented in an LUT.

Considering the drawbacks of the multifrequency approximation in [14] and the detailed loss modeling required in [15], the first contribution of this article is to propose a DCC strategy for the 3p-DAB based on a novel comprehensive piecewise time-domain analysis (TDA) and an optimization process that obtains the optimal control parameters for minimum rms phase current in buck and boost operation. By analyzing the phase voltage and inductor current waveforms, this article is the first to present the 18 TDA operating modes of a 3p-DAB with DCC defined by $D_1$, $D_2$, and $D_{ps}$. The nonlinear optimization problem to obtain the optimal control parameters is solved using MATLAB's Optimization Toolbox, and the results show that many of the 18 modes are not needed for optimal operation and can be eliminated, reducing the domain of the optimization problem, and simplifying its implementation. The theoretical results of this proposed TDA optimized modulation strategy (OMS) are validated experimentally.

The proposed straightforward TDA optimization, and the methods proposed in [14] and [15], rely on an offline optimization process with results being implemented in an LUT. Although optimal results can be obtained, downsides to this general approach include the fact that the optimization problem formulation and computation can be time-consuming, interpolation within an LUT can lead to error, and if a circuit parameter changes, the entire offline optimization process must be run again to generate a new LUT. A closed-form modulation scheme can overcome these drawbacks by calculating the optimal modulation parameters online in real time, using equations programmed into the microcontroller. A closed-form DCC modulation scheme for 3p-DAB, called asymmetrical DCC (ADCC), is proposed in [16] and similarly in [17]. By limiting the input and output bridge duty cycle range from 0 to 1/3 and adopting the triangular current mode and trapezoidal current mode, the authors in [16] and [17] propose a control that extends the soft-switching range of the 3p-DAB under light loads. However, since the duty cycles are limited, this control strategy does not cover the entire operating range, thus, large HSW regions still exist. Furthermore, Jiao et al. [18] proposed a closed-form modulation scheme based on a TDA using four variables ($D_1$, $D_2$, $D_{ps}$, and voltage gain), but this results in hundreds of operating modes, requiring simplifications and restrictions of the control mode; also, efficiency results are not provided to validate the resulting modulation scheme. Similarly, in [19], 108 unique operating modes are derived using a piecewise linear model for a three-level 3p-DAB with DCC. To reduce the number of operating modes and derive a closed-form minimum rms current modulation scheme, the control is simplified down to two degrees-of-freedom by approximating the duty cycle of the input-bridge switches to 0.5 during buck operation and the duty cycle of the output-bridge switches to 0.5 during boost operation. However, this results in rms phase currents 60% higher than the optimal control in some operating regions.

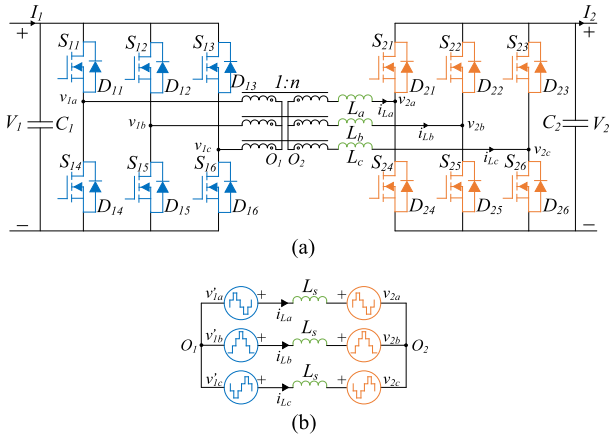


Fig. 1. Circuit schematic and equivalent circuit of the 3p-DAB. (a) Circuit schematic. (b) Equivalent circuit.

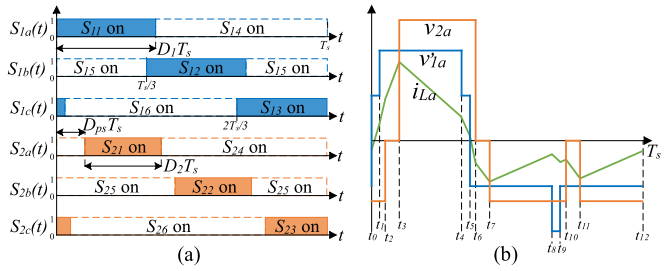


Fig. 2. Switch driving pulses and operating waveforms of the 3p-DAB with DCC. (a) Driving pulses. (b) Operating waveforms.

Thus, until now, no closed-form 3p-DAB DCC modulation scheme has been proposed in literature that can closely match the efficiency of an offline optimization-based scheme. The purpose of the second contribution of this article is to fill this gap by introducing a novel closed-form DCC modulation scheme for the 3p-DAB called the minimum current stress optimization (MCSO) scheme. The MCSO scheme is derived from the theoretical findings of the first contribution (proposed TDA optimization method). The experimental results show that this closed-form MCSO modulation scheme performs nearly identically to the OMS (which is based on the baseline DCC proposed in [14] but modified to use the more convenient TDA approach), meaning this is the first article to provide a closed-form DCC scheme for 3p-DAB that achieves efficiency results that are equivalent to a fully optimized offline scheme, but without the drawbacks of the offline optimization process and LUT implementation.

The rest of this article is organized as follows: Section II presents the TDA of the 3p-DAB with DCC, along with equations for the operating modes and their analytical expressions for average output power and rms phase current. Section III proposes the TDA optimization process and analyzes the results of the OMS for buck and boost operation. Section IV presents the novel closed-form modulation scheme, MCSO, which builds upon the TDA fundamentals derived in Section II. Section V presents the experimental results, verifying the exceptional performance of the proposed closed-form MCSO scheme compared to SPS, OMS, and the only other validated 3p-DAB closed-form DCC scheme from literature, the ADCC [16]. Finally, Section VI concludes this article.

## II. Time-Domain Analysis of 3P-DAB With Duty Cycle Control

### A. Overview of 3P-DAB With Duty Cycle Control

Fig. 1(a) illustrates the circuit schematic of a 3p-DAB converter and Fig. 1(b) shows the corresponding equivalent circuit. $V_1$ and $V_2$ are the input and output dc voltages, $I_1$ and $I_2$ are the input and output dc currents, and $C_1$ and $C_2$ are the input and output filter capacitances, respectively. The input bridge is composed of switches $S_{11}$–$S_{16}$ and the output bridge is composed of switches $S_{21}$–$S_{26}$. Connecting the two active bridges together is a balanced three-phase high-frequency Y–Y transformer with turns ratio *1:n*. Inductors $L_a$, $L_b$, and $L_c$ are equal and represent the transformer leakage inductance. $i_{La}$, $i_{Lb}$, and $i_{Lc}$ are the inductor currents; $v_{1a}$, $v_{1b}$, and $v_{1c}$ are the primary side phase voltages; and $v_{2a}$, $v_{2b}$, and $v_{2c}$ are the secondary side phase voltages. The analysis carried out in this article assumes all components are ideal, thus parasitic resistances, inductances, and capacitances are not considered. Furthermore, due to the balanced and symmetrical nature of the 3p-DAB topology, only a single phase and power flow in the forward direction needs to be considered for a complete analysis. The switch driving pulses and corresponding phase voltage and inductor current waveforms for the 3p-DAB with DCC are shown in Fig. 2. Fig. 2(a) shows that the driving pulses for each phase leg are complementary, and phase shifted by $T_s/3$, where $T_s$ is the converter's switching period. The duration of a switching period that $S_{11}$, $S_{12}$, and $S_{13}$ are ON is variable and denoted by $D_1T_s$. Similarly, the duration of a switching period that $S_{21}$, $S_{22}$, and $S_{23}$ are ON is variable and denoted by $D_2T_s$. Lastly, the phase shift between the rising edges of the driving pulses of the input and output bridges is variable and denoted by $D_{ps}T_s$. Thus, $D_1$, $D_2$, and $D_{ps}$ are the control parameters for the 3p-DAB under DCC and the range of values that they can take are given in (1). It is a common practice with DAB converters to limit the range of $D_{ps}$ because of the excessive reactive power that high magnitude phase-shift ratios create [20]. Thus, this article poses a practical limit of 1/6 on $D_{ps}$.

The phase voltages $v'_{1a}$ (secondary referred) and $v_{2a}$ are shown in Fig. 2(b). It is beneficial to define the switching function $S_{xy}(t)$ for the six phase legs of the 3p-DAB, where ($x = 1, 2$, $y = a, b, c$). $S_{xy}(t)$ takes the value of 1 when a topside switch of a phase leg is ON and the value of 0 when a bottom side switch of a phase leg is ON. For example, referring to Fig. 2(a), $S_{2a}(t)$ is the switching function for phase leg A in the output bridge and it takes the value of 1 at time $D_{ps}T_s$ for the duration of $D_2T_s$ and takes the value of 0 for the duration of $(1 - D_2)T_s$. Since the switches in a phase leg are complementary, $S_{xy}(t)$ will either be 1 or 0, thus ambiguity in the function is avoided. Using $S_{xy}(t)$, the six-step phase voltage waveforms of the input and output

bridge can be derived and are shown as (2) and (3):

$$\begin{cases} 0 \le D_1 \le 1/2 \\ 0 \le D_2 \le 1/2 \\ 0 \le D_{ps} \le 1/6 \end{cases} \tag{1}$$

$$\begin{cases} v'_{1a}(t) = \frac{nV_1[2S_{1a}(t)-S_{1b}(t)-S_{1c}(t)]}{3} \\ v'_{1b}(t) = \frac{nV_1[2S_{1b}(t)-S_{1a}(t)-S_{1c}(t)]}{3} \\ v'_{1c}(t) = \frac{nV_1[2S_{1c}(t)-S_{1a}(t)-S_{1b}(t)]}{3} \end{cases} \tag{2}$$

$$\begin{cases} v_{2a}(t) = \frac{\mathrm{ndV}_1[2S_{2a}(t)-S_{2b}(t)-S_{2c}(t)]}{3} \\ v_{2b}(t) = \frac{\mathrm{ndV}_1[2S_{2b}(t)-S_{2a}(t)-S_{2c}(t)]}{3} \\ v_{2c}(t) = \frac{\mathrm{ndV}_1[2S_{2c}(t)-S_{2a}(t)-S_{2b}(t)]}{3}. \end{cases} \tag{3}$$

During steady-state operation the phase voltages are periodic, and average to zero over a switching period. Using the equivalent circuit model in Fig. 1(b), the expression for the inductor current can be derived as (4), where $t_o$ denotes the beginning of the switching period and $L_s$ is the series inductance in phase A. Assuming a balanced three-phase transformer, the equations of rms inductor current and total average transmission power can then be expressed using phase A quantities as (5) and (6), respectively,

$$i_{La}(t) = i_{La}(t_0) + \frac{1}{L_s}\int_{t_0}^{t} [v'_{1a}(\tau) - v_{2a}(\tau)]\, d\tau \tag{4}$$

$$I_{\mathrm{Lrms}} = \sqrt{\frac{1}{T_s}\int_0^{T_s} i_{La}^2(t)\, dt} \tag{5}$$

$$P_o = \frac{3n}{T_s}\int_0^{T_s} v_{1a}(t)\, i_{La}(t)\, dt. \tag{6}$$

### B. Time Domain Analysis – Operating Modes

The preceding analysis shows that the output power and phase current expressions of the 3p-DAB with DCC are piecewise-linear and dependent on the control parameters $D_1$, $D_2$, and $D_{ps}$. Consequently, this creates various modes of operation for the 3p-DAB within the domain of DCC described by (1). Since a TDA of the 3p-DAB with DCC has yet to be conducted in existing literature, Fig. 3 illustrates for the first time that there are 18 different operating modes for the 3p-DAB under DCC with control parameters $D_1$, $D_2$, and $D_{ps}$. Each operating mode is characterized by the set of control parameters that yield an inductor voltage waveform of the same step sequence. As a result, each operating mode requires a unique set of analytic expressions to model its operation. It is useful to visualize the operating modes as the 3-D regions of space that the intersections of eight boundary planes, shown in Fig. 3, create within the domain of (1). Table I presents a summary of the operating mode regions expressed mathematically as inequalities of the control parameters $D_1$, $D_2$, and $D_{ps}$, which will be used to define the analytical expressions for each mode.

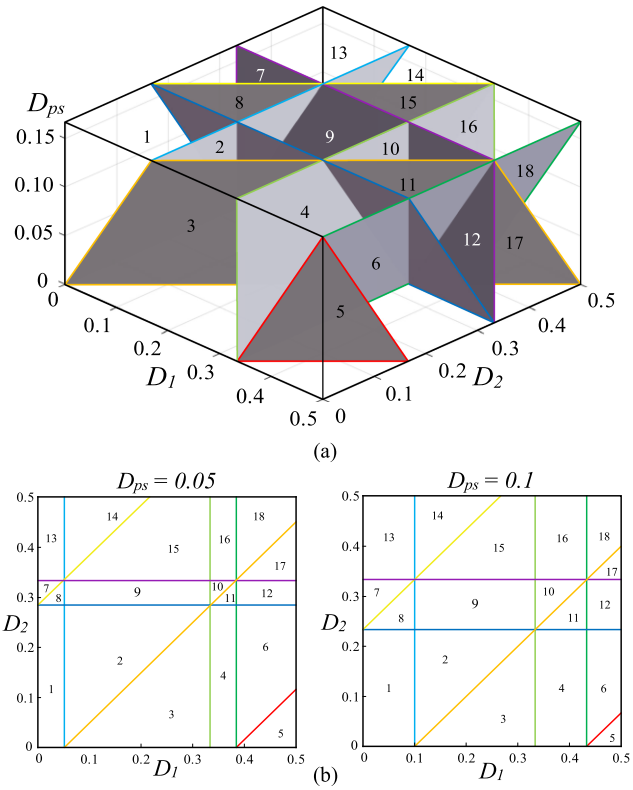


Fig. 3. Operating mode boundaries for the 3p-DAB with DCC. (a) 3-D illustration. (b) Cross section view of operating modes at fixed phase shift ratios.

TABLE I
CONTROL PARAMETER LIMITS FOR OPERATING MODES

| Mode | Limits on $D_1$ | Limits on $D_2$ |
|---|---|---|
| 1 | $0 < D_1 < D_{ps}$ | $0 < D_2 < (-D_{ps} + 1/3)$ |
| 2 | $D_{ps} < D_1 < (D_2 + D_{ps})$ | $(D_1 - D_{ps}) < D_2 < (-D_{ps} + 1/3)$ |
| 3 | $(D_2 + D_{ps}) < D_1 < 1/3$ | $0 < D_2 < (D_1 - D_{ps})$ |
| 4 | $1/3 < D_1 < (D_{ps} + 1/3)$ | $0 < D_2 < (-D_{ps} + 1/3)$ |
| 5 | $(D_2 + D_{ps} + 1/3) < D_1 < 1/2$ | $0 < D_2 < (D_1 - D_{ps} - 1/3)$ |
| 6 | $(D_{ps} + 1/3) < D_1 < (D_2 + D_{ps} + 1/3)$ | $(D_1 - D_{ps} - 1/3) < D_2 < (-D_{ps} + 1/3)$ |
| 7 | $0 < D_1 < (D_2 + D_{ps} - 1/3)$ | $(D_1 - D_{ps} + 1/3) < D_2 < 1/3$ |
| 8 | $(D_2 + D_{ps} - 1/3) < D_1 < D_{ps}$ | $(-D_{ps} + 1/3) < D_2 < (D_1 - D_{ps} + 1/3)$ |
| 9 | $D_{ps} < D_1 < 1/3$ | $(-D_{ps} + 1/3) < D_2 < 1/3$ |
| 10 | $1/3 < D_1 < (D_2 + D_{ps})$ | $(D_1 - D_{ps}) < D_2 < 1/3$ |
| 11 | $(D_2 + D_{ps}) < D_1 < (D_{ps} + 1/3)$ | $(-D_{ps} + 1/3) < D_2 < (D_1 - D_{ps})$ |
| 12 | $(D_{ps} + 1/3) < D_1 < 1/2$ | $(-D_{ps} + 1/3) < D_2 < 1/3$ |
| 13 | $0 < D_1 < D_{ps}$ | $1/3 < D_2 < 1/2$ |
| 14 | $D_{ps} < D_1 < (D_2 + D_{ps} - 1/3)$ | $(D_1 - D_{ps} + 1/3) < D_2 < 1/2$ |
| 15 | $(D_2 + D_{ps} - 1/3) < D_1 < 1/3$ | $1/3 < D_2 < (D_1 - D_{ps} + 1/3)$ |
| 16 | $1/3 < D_1 < (D_{ps} + 1/3)$ | $1/3 < D_2 < 1/2$ |
| 17 | $(D_2 + D_{ps}) < D_1 < 1/2$ | $1/3 < D_2 < (D_1 - D_{ps})$ |
| 18 | $(D_{ps} + 1/3) < D_1 < (D_2 + D_{ps})$ | $(D_1 - D_{ps}) < D_2 < 1/2$ |
| *For all operating modes*: $0 < D_{ps} < 1/6$ | | |

### C. Time Domain Analysis – Analytical Expressions

Fig. 4 illustrates examples of each operating mode's phase voltage and inductor current waveforms. To use piecewise modeling to describe the 3p-DAB with DCC, a TDA must be carried out for each of the 18 operating modes to obtain expressions

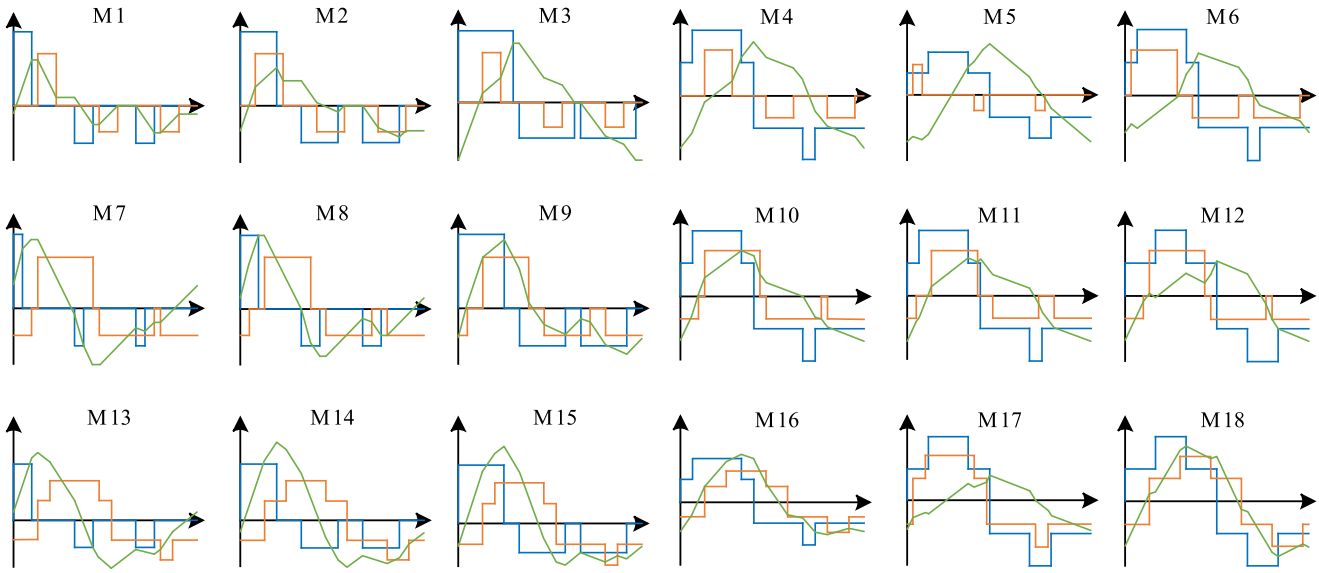


Fig. 4. Operating waveforms during one switching period for the 18 operating modes of DCC. Blue: $v'_{1a}(t)$, Orange: $v_{2a}(t)$, and Green: $i_{la}(t)$.

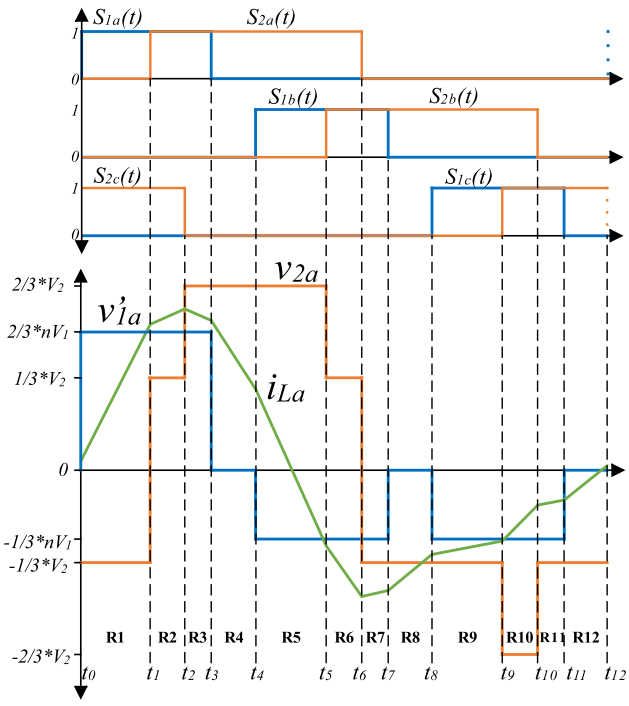


Fig. 5. Driving pulses and operating waveforms for a 3p-DAB operating with DCC.

for $P_{\text{out}}$ and $I_{\text{LRMS}}$. This section demonstrates the TDA for Mode 15 (M15), however, the same process can be applied to the other modes of operation, and the results for the selected optimal operating modes are shown in Appendix A.

To facilitate the analysis, Fig. 5 presents the switch driving pulses and operating waveforms for M15. Within the boundaries of all operating modes, the phase current waveforms are asymmetric, periodic, and composed of 12 linear regions R1 to R12. The instances in a switching period where a switch turns ON or OFF are denoted by $t_0$, $t_1$, … $t_{11}$ and can be expressed using $D_1$, $D_2$, and $D_{ps}$. Using (4), the piecewise time-domain expressions of the phase A current for M15 can be constructed, as shown in Table II. Since the phase currents must average to zero over one switching period during steady-state operation, the initial condition for the phase current $i_{La}(t_0)$ can be solved using (7). Table III shows the solved piecewise expressions for M15 phase current.

TABLE II
OPERATING CURRENT EXPRESSIONS FOR MODE 15

| Region | Interval Start Time | Expression of $i_{La}$ |
|---|---|---|
| R1 | $t_0 = t_{12} = 0$ | $i_{La}(t_0) + k(2+d)(t-t_0)$ |
| R2 | $t_1 = D_{ps}$ | $i_{La}(t_1) + k(2-d)(t-t_1)$ |
| R3 | $t_2 = D_2 + D_{ps} - 1/3$ | $i_{La}(t_2) + 2k(1-d)(t-t_2)$ |
| R4 | $t_3 = D_1$ | $i_{La}(t_3) - 2kd(t-t_3)$ |
| R5 | $t_4 = 1/3$ | $i_{La}(t_4) - k(1+2d)(t-t_4)$ |
| R6 | $t_5 = 1/3 + D_{ps}$ | $i_{La}(t_5) - k(1+d)(t-t_5)$ |
| R7 | $t_6 = D_2 + D_{ps}$ | $i_{La}(t_6) - k(1-d)(t-t_6)$ |
| R8 | $t_7 = 1/3 + D_1$ | $i_{La}(t_7) + kd(t-t_7)$ |
| R9 | $t_8 = 2/3$ | $i_{La}(t_8) - k(1-d)(t-t_8)$ |
| R10 | $t_9 = 2/3 + D_{ps}$ | $i_{La}(t_9) - k(1-2d)(t-t_9)$ |
| R11 | $t_{10} = 1/3 + D_2 + D_{ps}$ | $i_{La}(t_{10}) - k(1-d)(t-t_{10})$ |
| R12 | $t_{11} = 2/3 + D_1$ | $i_{La}(t_{11}) + kd(t-t_{11})$ |

$$\textit{where} \quad k = \frac{nV_1}{3L_s f_s}, \quad d = \frac{V_2}{nV_1}$$

$$\int_{t_0}^{t_{12}} i_L(\tau)\, d\tau = 0. \tag{7}$$

The average output current expression for M15 can be constructed by analyzing the switching sequence of the output bridge switching functions $S_{2a}$(t), $S_{2b}$(t), and $S_{2c}(t)$ during 1/3 of a switching period, i.e., regions R1 to R4 or equivalently, $t_0$ to $t_4$ as notated in Fig. 5. In region R1, only $S_{2c}(t)$ is ON, thus, the output current during this interval is $i_{Lc1}(t)$. So far, the phase current expressions developed in this research have been for phase A, however, it is possible to determine the phase

TABLE III
SOLVED OPERATING CURRENT EQUATIONS FOR MODE 15

| Region | Expression of $I_a$ for Mode 15 |
|---|---|
| R1 | $i_{La1}(t) = k(6t + d - 3D_1 + 3dt - 3dD_{ps})/3$ |
| R2 | $i_{La2}(t) = k(6t + d - 3D_1 - 3dt + 3dD_{ps})/3$ |
| R3 | $i_{La3}(t) = k(2t - D_1 - 2dt + dD_2 + 2dD_{ps})$ |
| R4 | $i_{La4}(t) = k(D_1 - 2dt + dD_2 + 2dD_{ps})$ |
| R5 | $i_{La5}(t) = k(1 - 3t + 3D_1 - 6dt + 3dD_2 + 6dD_{ps})/3$ |
| R6 | $i_{La6}(t) = k(1 - 3t - d + 3D_1 - 3dt + 3dD_2 + 3dD_{ps})/3$ |
| R7 | $i_{La7}(t) = k(1 - 3t - d + 3D_1 + 3dt - 3dD_2 - 3dD_{ps})/3$ |
| R8 | $i_{La8}(t) = k(3t - 1 - 3D_2 - 3D_{ps})/3$ |
| R9 | $i_{La9}(t) = k(2 - 3t - d + 3dt - 3dD_2 - 3dD_{ps})/3$ |
| R10 | $i_{La10}(t) = k(2 - 3t - 3d + 6dt - 3dD_2 - 6dD_{ps})/3$ |
| R11 | $i_{La11}(t) = k(2 - 3t - 2d + 3dt - 3dD_{ps})/3$ |
| R12 | $i_{La12}(t) = k(3dt - 2d - 3D_1 - 3dD_{ps})/3$ |
| | **where** $\boldsymbol{k = \frac{nV_1}{3L_s f_s}}$, $\boldsymbol{d = \frac{V_2}{nV_1}}$ |

B and phase C current expressions from phase A by delaying the phase A current waveform by 120° and 240°, respectively. Therefore, $i_{Lc1}(t)$ is equivalent to $i_{La5}(t)$. In R2, only $S_{2a}(t)$ and $S_{2c}(t)$ are ON, thus, the output current during this interval is the sum of $i_{La2}(t)$ and $i_{Lc2}(t) = i_{La6}(t)$. In R3 and R4, only $S_{2a}(t)$ is ON, thus, the output current during these intervals is equivalent to $i_{La3}(t)$ and $i_{La4}(t)$, respectively. The resulting expression for the average output current for M15 is provided in (8). Solving (8) and multiplying it with the output voltage $V_2 = ndV_1$, the average output power expression for M15 can be obtained, as shown in (9). The equation for the rms phase current of M15 can be derived by substituting the 12 piecewise equations from Table III into (5) and solving the integral. The result is shown in (10). It is worth mentioning that operating in M5 and M6 results in negative average power transfer, meaning that power flows from the output bridge to the input bridge because of the large difference between control parameters $D_1$ and $D_2$. Because of this, M5 and M6 are not analyzed in detail.

$$I_{\text{out}_{M15}} = 3\left(\int_{t_4}^{t_5} i_{La5}(\tau)\,d\tau + \int_{t_1}^{t_2} i_{La2}(\tau)\,d\tau + \int_{t_5}^{t_6} i_{La6}(\tau)\,d\tau + \int_{t_2}^{t_3} i_{La3}(\tau)\,d\tau + \int_{t_3}^{t_4} i_{La4}(\tau)\,d\tau\right) \tag{8}$$

$$P_{\text{out}_{M15}} = \frac{V_1^2 n^2 d}{18L_s f_s}\left(-18D_1^2 + 18D_1D_2 + 36D_1D_{ps} - 9D_2^2 - 18D_2D_{ps} + 6D_2 - 27D_{ps}^2 + 6D_{ps} - 1\right) \tag{9}$$

$$\begin{aligned} I_{\text{LRMS}_{M15}} = \frac{V_1 n}{9\sqrt{3}L_s f_s}\big(&9d^2D_2 - 9d^2D_2^2 - d^2 + 54dD_1^3 \\ &- 81dD_1^2D_2 - 162dD_1^2D_{ps} + 81dD_1D_2^2 \\ &+ 162dD_1D_2D_{ps} - 36dD_1D_2 + 162dD_1D_{ps}^2 \\ &- 27dD_2^3 - 81dD_2^2D_{ps} + 27dD_2^2 - 81dD_2D_{ps}^2 \\ &+ 54dD_2D_{ps} - 9dD_2 - 81dD_{ps}^3 + 27dD_{ps}^2 \\ &- 9dD_{ps} + d - 27D_1^3 + 18D_1^2\big)^{1/2}. \end{aligned} \tag{10}$$

## III. PROPOSED OPTIMIZATION STRATEGY

Optimizing the control parameters $D_1$, $D_2$, and $D_{ps}$ for minimum conduction loss across all operating points ($d$, $P_{\text{ref}}$) means that the ohmic losses of the semiconductor devices, high-frequency transformer, and PCB traces are minimized. Since the ohmic losses for a 3p-DAB are proportional to the square of the rms phase current ($I_{\text{Lrms}}^2$) it leads to the optimization problem given by (11). The nature of the objective and equality constraint functions is piecewise smooth across the domain of DCC; thus, an optimization problem must be defined for each operating mode using the expressions derived in Section II. The objective function ensures that the ohmic losses are minimized, the nonlinear equality constraint ensures that the operating point ($d$, $P_{\text{ref}}$) is satisfied, and the linear inequality constraints constrain $D_1$, $D_2$, and $D_{ps}$ to the domain of the operating mode $j$ that both the objective function and equality constraint belong to

$$\begin{aligned} &\min\ {I_{\text{LRMSj}}}^2\ (D_1, D_2, D_{ps}, d) \\ &\text{Subject to} \\ &P_{\text{outj}}(D_1, D_2, D_{ps}, d) - P_{\text{ref}} = 0 \\ &A_j \boldsymbol{X} \le b_j,\ \textit{where}\ \boldsymbol{X} = \begin{bmatrix} D_1 \\ D_2 \\ D_{ps} \end{bmatrix}, 1 \le j \le 18. \end{aligned} \tag{11}$$

The active-set method from MATLAB's Optimization Toolbox was implemented to solve the nonlinear optimization problem for each mode. Then, the global optimal control parameters were obtained by means of comparison to determine which mode's optimal control yielded the lowest rms phase current for a given operating point ($d$, $P_{\text{ref}}$). The optimal control surfaces for $D_1$, $D_2$, and $D_{ps}$ are shown in Fig. 6, where the voltage gain $d$ ranges from 0.5 (buck) to 1.5 (boost) and the output power is normalized to $P_{\text{base}} = {V_1}^2 n^2/(12L_s f_s)$. Fig. 7(a) and (b) show curves of the control parameters for buck and boost operation, where the voltage gain $d$ is fixed to 0.6 and 1.4, respectively. Fig. 7(c) and (d) show the corresponding rms phase currents normalized to $I_{\text{base}} = V_1 n/(12L_s f_s)$, and highlights the theoretical improvement of the proposed OMS over SPS control through the significant reduction of the rms phase current during low-to-medium power transmission.

Analyzing the optimized control parameters reveals that only 5 of the 18 DCC operating modes contribute to the OMS, and thus, the remaining modes can be considered suboptimal and are therefore redundant. This can be observed through Fig. 8 which shows curves for each operating mode's locally minimized rms phase current as a function of output power during buck operation ($d = 0.6$), where the optimal modes are shown in bold. As shown in Fig. 8 for buck operation, operating in M2 during low power until the M2 boundary, M15 during medium power until the M15 boundary, and M16 during high power, achieves the globally minimized rms phase currents across the entire output power range. A similar analysis for boost operation shows that globally minimized rms phase current across the entire output power range can be achieved by operating in M3 during low power, M10 during medium power, and M16 during high power.

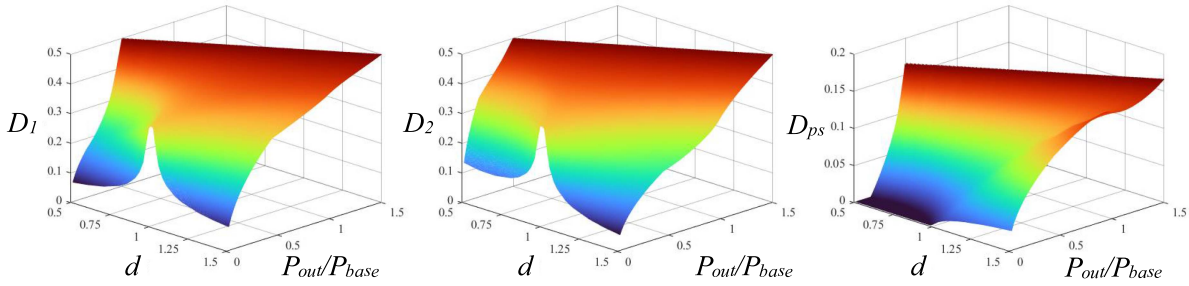


Fig. 6. Optimized control parameter surfaces to achieve minimum rms phase current in buck and boost operation.

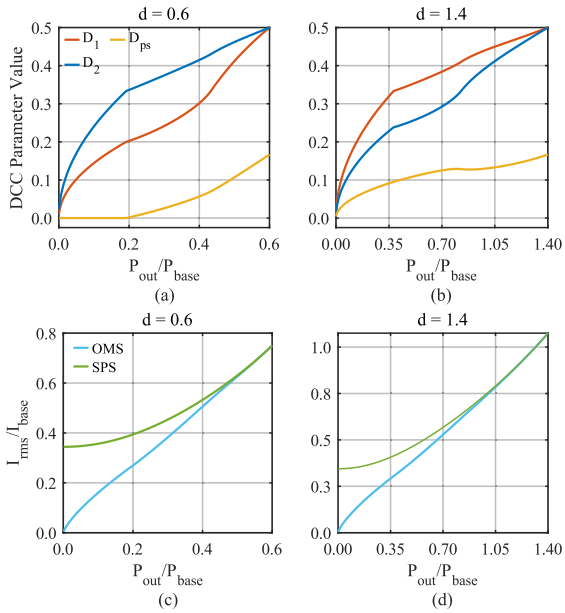


Fig. 7. (a) and (b) 2-D curves of OMS control parameters with fixed voltage gain. (c) and (d) Comparison of RMS phase current: SPS versus OMS.

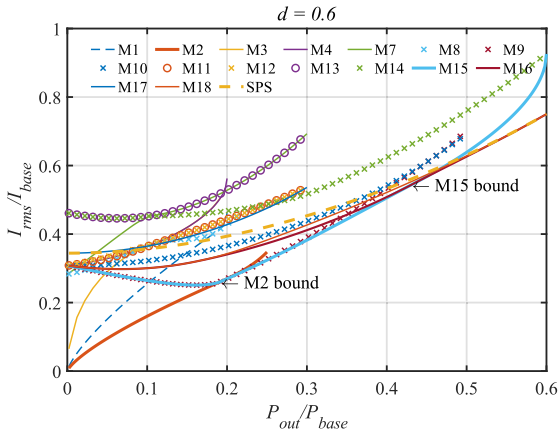


Fig. 8. Locally minimized rms current curves for each DCC operating mode for buck operation ($d = 0.6$). M2, M15, and M16 achieve global minimum rms phase current for entire output power range.

Fig. 9 shows the upper and lower power boundaries for each of the five optimal operating modes in the OMS and was derived by repeating the minimum rms phase current optimization process that gave Fig. 8, for all voltage gain values ($0.5 < d < 1.5$). For example, by analyzing the operating points ($d$, $P_o$), where M2's rms phase current intersects M15's rms phase current and where M15's rms phase current intersects M16's rms phase current, the upper and lower power boundaries of M2, M15, and M16 were obtained.

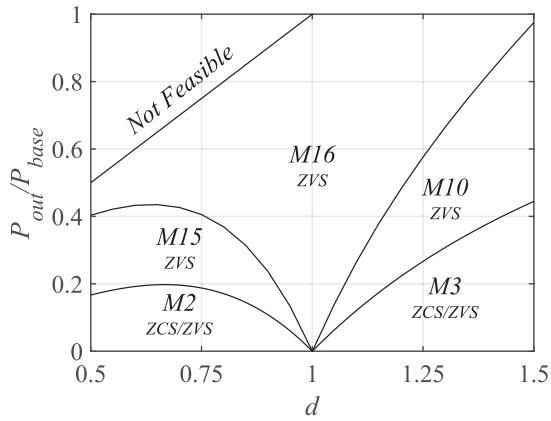


Fig. 9. Operating modes and turn-ON soft-switching characteristics of OMS scheme in terms of voltage gain $d$ and output power normalized to $P_{\text{base}}$.

## IV. Proposed Closed-Form Modulation Scheme

The novel TDA and offline optimization process presented in Sections II and III are used as the theoretical basis for the proposed closed-form MCSO scheme presented as follows. Using the closed-form equations derived as follows, this MCSO scheme can be programmed into a microcontroller to calculate optimal DCC parameters in real time during converter operation. To construct the closed-form MCSO scheme over the entire buck and boost operating range, the five operating modes in Fig. 9 are discussed and analyzed in the following subsections.

### A. M2 – Low-Power Buck Operation ($0.5 < d < 1$)

According to the OMS, the 3p-DAB operates in M2 during low-power buck operation. Analyzing the numerical solutions of the optimized control parameters in M2 from Fig. 6 (also shown in Fig. 7(a) for $d = 0.6$) reveals that for optimal operation in M2, $D_{ps} = 0$ and $D_1 = dD_2$. Substituting these into the average output power expression for M2 (12) gives the closed-form expression for $D_2$ (13) in terms of $P_{\text{out}}$, $d$, and converter parameters to achieve minimum rms phase current. The maximum power transfer while operating in M2 is presented in (14) and can be

deduced from (12) by realizing that at the upper power boundary of M2, $D_2$ is always equal to *1/3*

$$P_{\text{out}_{M2}} = \frac{dV_1^2 n^2}{L_s f_s}\left(2D_1 D_{ps} - D_1^2 + D_2 D_1 - D_{ps}^2\right) \quad (12)$$

$$\begin{cases} D_2 = \sqrt{\frac{P_{\text{out}} L_s f_s}{d^2 V_1^2 n^2 (1-d)}} \\ D_1 = dD_2 \\ D_{ps} = 0 \end{cases} \quad (13)$$

$$0 < P_{\text{out}} < \frac{V_1^2 d^2 n^2 (1-d)}{9 L_s f_s}. \quad (14)$$

### *B. M3 – Low-Power Boost Operation (1 < d < 1.5)*

Similarly, according to the OMS, the 3p-DAB operates in M3 during low-power boost operation. Analyzing the numerical solutions of the optimized control parameters in M3 from Fig. 6 (also shown in Fig. 7(b) for $d = 1.4$) reveals that $D_2 = D_{ps}/(d-1)$ and $D_1 = dD_2$ for optimal operation in M3. Substituting these into the average output power expression for M3 (15) allows derivation of the closed-form expression for $D_{ps}$ (16) in terms of $P_{\text{out}}$, $d$, and converter parameters to achieve minimum rms phase current. The maximum power transfer while operating in M3 is presented in (17) and can be deduced from (15) by realizing that at the upper boundary of M3, $D_1$ is always equal to 1/3

$$P_{\text{out}_{M3}} = \frac{dV_1^2 n^2 D_2}{L_s f_s}\left(D_2 - D_1 + 2D_{ps}\right) \quad (15)$$

$$\begin{cases} D_{ps} = (d-1)\sqrt{\frac{P_{\text{out}} L_s f_s}{dV_1^2 n^2 (d-1)}} \\ D_2 = \frac{D_{ps}}{(d-1)} \\ D_1 = dD_2 \end{cases} \quad (16)$$

$$0 < P_{\text{out}} < \frac{V_1^2 n^2 (d-1)}{9 d L_s f_s}. \quad (17)$$

### *C. M15 – Medium-Power Buck Operation (0.5 < d < 1)*

According to the OMS, the 3p-DAB operates in M15 during medium-power buck operation. Analyzing the numerical solutions of the optimized control parameters in M15 from Fig. 7(a) reveals no apparent parametrization of the optimal control variables, thus closed-form solutions for the control parameters in M15 cannot be obtained like they were for M2 and M3. Therefore, instead of using rms phase current as the objective function, current stress is used to conveniently allow for an analytical optimization using the global optimal conditions (GOC) proposed in [17] due to the linear nature of the peak current expressions of the 3p-DAB. The GOC for MCS for a 3p-DAB with DCC is defined in (18) as

$$\frac{\frac{\partial i_{p_{Mj}}}{\partial D_1}}{\frac{\partial P_{Mj}}{\partial D_1}} = \frac{\frac{\partial i_{p_{Mj}}}{\partial D_2}}{\frac{\partial P_{Mj}}{\partial D_2}} = \frac{\frac{\partial i_{p_{Mj}}}{\partial D_{ps}}}{\frac{\partial P_{Mj}}{\partial D_{ps}}} \quad (18)$$

where $i_{PMj}$ is the expression for the peak current in Mode $j$, and $P_{Mj}$ is the expression for average output power in Mode $j$. While operating in M15, the average output power and peak current expressions are given by (9) and (19), respectively. Computing their partial derivatives with respect to $D_1$, $D_2$, and $D_{ps}$ and substituting them into the GOC (18) yields the system of equations given by (20). Solving (20) yields expressions for $D_1$ and $D_2$ in terms of $D_{ps}$ and can be substituted into (9) to solve for the expression of $D_{ps}$ in terms of $P_{\text{out}}$, $d$, and converter parameters. The resulting closed-form control parameters to achieve MCS in M15 are given by (21). The upper power boundary of M15, as shown in Fig. 9, does not have a closed-form expression, thus a fourth-order polynomial is fit to the curve to define the upper power boundary of M15 (22)

$$i_{p_{M15}} = \frac{V_1 n}{3 L_s f_s}\left(D_1 - 2dD_1 + dD_2 + 2dD_{ps}\right) \quad (19)$$

$$\frac{1-2d}{3d\left(D_2 - 2D_1 + 2D_{ps}\right)} = \frac{1}{3D_1 - 3D_2 - 3D_{ps} + 1} = \frac{2}{6D_1 - 3D_2 - 9D_{ps} + 1} \quad (20)$$

$$\begin{cases} D_{ps} = \frac{1}{3} - \frac{\sqrt{d\left(V_1^2 n^2 d - 9 L_s f_s P_{\text{out}}\right)}}{3V_1 n d\sqrt{d^2 - d + 1}} \\ D_1 = (2-d) D_{ps} + \frac{d}{3} \\ D_2 = D_{ps} + \frac{1}{3} \end{cases} \quad (21)$$

$$\frac{P_{\text{out}}}{P_{\text{base}}} < \begin{bmatrix} -2.779 & 4.526 & -3.891 & 2.319 & -0.175 \end{bmatrix} \begin{bmatrix} d^4 \\ d^3 \\ d^2 \\ d^1 \\ d^0 \end{bmatrix}. \quad (22)$$

### *D. M10 – Medium Power Boost Operation (1 < d < 1.5)*

Similarly, according to the OMS, the 3p-DAB operates in M10 during medium power boost operation. Analyzing the numerical solutions of the optimized control parameters in M10 from Fig. 7(b) reveals no apparent parametrization of the optimal control variables, thus closed-form solutions for the optimal control parameters in M10 cannot be obtained like they were for M2 and M3. Again, instead of using rms phase current as the objective function, current stress is used to conveniently allow for an analytical optimization using the GOC. While operating in M10, the average output power and peak current expressions are given by (9) and (23), respectively. Computing their partial derivatives with respect to $D_1$, $D_2$, and $D_{ps}$ and substituting them into (18) yields the system of equations given by (24). Solving (24) yields expressions for $D_1$ and $D_2$ in terms of $D_{ps}$ and can be substituted into (9) to solve for the expression of $D_{ps}$ in terms of $P_{\text{out}}$, $d$, and converter parameters. The resulting closed-form control parameters to achieve MCS in M10 are given in (25). The upper power boundary of M10, as shown in Fig. 9, does not have a closed-form expression, thus a fourth-order polynomial is fit to the curve to define the upper power boundary of M10 (26).

$$i_{p_{M10}} = \frac{V_1 n}{3 L_s f_s}\left(-D_1 + dD_2 + 2D_{ps}\right) \quad (23)$$

$$\frac{-1}{3d\left(D_2 - 2D_1 + 2D_{ps}\right)} = \frac{1}{3D_1 - 3D_2 - 3D_{ps} + 1} = \frac{12}{d\left(36D_1 - 18D_2 - 54D_{ps} + 6\right)} \quad (24)$$

$$\begin{cases} D_{ps} = \frac{1}{3} - \frac{\sqrt{d\left(V_1^2 n^2 d - 9L_s f_s P_{\text{out}}\right)}}{3V_1 n d\sqrt{d^2-d+1}} \\ D_1 = dD_{ps} - \frac{d}{3} + \frac{2}{3} \\ D_2 = (2d-1)D_{ps} - \frac{2d}{3} + 1 \end{cases} \tag{25}$$

$$\frac{P_{\text{out}}}{P_{\text{base}}} < \begin{bmatrix} -2.779 & 15.748 & -34.469 & 35.706 & -14.229 \end{bmatrix} \begin{bmatrix} d^4 \\ d^3 \\ d^2 \\ d^1 \\ d^0 \end{bmatrix}. \tag{26}$$

### E. M16 – High Power Operation ($0.5 < d < 1.5$)

According to the OMS, the 3p-DAB operates in M16 during high power buck and boost operation. Analyzing the numerical solutions of the optimized control parameters in M16 from Fig. 7(a) and (b) reveals no apparent parametrization of the optimal control variables, thus closed-form solutions for the optimal control parameters in M16 cannot be obtained like they were for M2 and M3. However, close inspection of Fig. 7(c) and (d) in the region of M16 reveals that the rms phase current of SPS is almost equal to the rms phase current of the OMS, and in fact the magnitude of the rms phase current of the OMS converges to SPS when the voltage gain is close to unity or when the power transfer is large. Because of this, the proposed modulation scheme, MCSO, operates the 3p-DAB using SPS in M16. The closed-form control parameters for SPS modulation are provided in (27) and the upper power boundary is given in (28) when $D_{ps} = 1/6$

$$\begin{cases} D_{ps} = \frac{1}{3} - \frac{1}{3}\sqrt{1 - \frac{9L_s f_s P_{\text{out}}}{V_1^2 n^2 d}} \\ D_1 = D_2 = \frac{1}{2} \end{cases} \tag{27}$$

$$P_{\text{out}} < \frac{V_1^2 n^2 d}{12 L_s f_s}. \tag{28}$$

### F. Summary of MCSO Operation

This subsection discusses the notable features of the proposed MCSO scheme which contribute to its excellent performance. Furthermore, Appendix B provides the mathematical analysis of the turn-ON soft-switching conditions for a 3p-DAB operating with MCSO.

When operating in M2 and M3, the phase current waveforms are triangular, which simultaneously achieves both minimum rms phase current and minimum peak current, and all switches experience either zero-current switching (ZCS) or zero-voltage switching (ZVS) at turn-ON. Operating the 3p-DAB with triangular phase currents during low power operation has been discussed previously in [14] and [16], however, in [16] it was not concluded if in fact minimum rms current operation was achieved and in [14] analysis of the low power boost operation was not considered (i.e., M3 of the proposed MCSO) and no closed-form expressions for the control parameters were provided.

During medium power transmission and wide voltage variation, the proposed MCSO modulation scheme operates in M15 for buck voltage gains and M10 for boost voltage gains. While operating in these modes, local MCS is achieved which reduces the magnitude of the rms phase current when compared to SPS. In addition, while operating in M15 and M10, all switches experience ZVS at turn-ON, whereas if operating using SPS, hard switching (HSW) would occur in either the primary or secondary bridge.

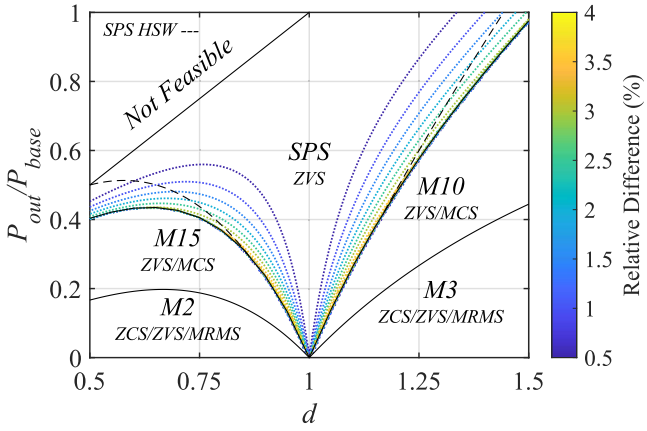


Fig. 10. Annotated operating mode regions of the MCSO modulation scheme in terms of voltage gain $d$ and output power normalized to $P_{base}$. The "relative difference" contour lines show the increase in RMS phase current at different operating points by using SPS instead of M16 (to achieve a closed-form equation).

During high power transmission and buck or boost voltage gain, the proposed MCSO modulation scheme operates the 3p-DAB using SPS. In this region, SPS produces rms phase currents very close to the global minimum and achieves ZVS at turn-ON for the vast majority of the operating region except for the two small regions above M15 and M10. Fig. 10 summarizes the features of each operating mode of the proposed MCSO modulation scheme. It also shows that the substitution of SPS for M16 results in a worst-case increase of rms phase current of about 4% in two very small slivers of operation area near the upper boundaries of M15 and M10, with most of the points near the boundaries having less than 2.5% increase of rms phase current compared to M16. As the output power increases, the minimized currents of M16 converge to SPS which can be seen as the contour lines approach zero. Combined, these features allow the proposed closed-form MCSO modulation scheme to achieve nearly identical efficiencies as the OMS under wide voltage and power variations.

Like all closed-form schemes, the MCSO modulation scheme can be applied to other 3p-DAB converters with a different switching frequency, power level, voltage level, transformer turns ratio, or leakage inductance because the closed-form DCC expressions [(13), (16), (21), (25), and (27)] consider these parameters in their calculation. Since the power boundaries of M10 and M15 [(22) and (26)] required a polynomial fit, other converters must either use the same common design rule for $L_s$ as used in this research, or numerically find these boundaries for a different design rule. In this research, the common approach from [22] is used for setting $L_s$, which ensures that maximum power is transferred at maximum phase shift and unity voltage gain.

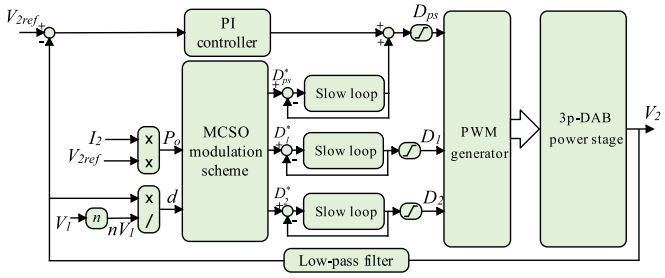


Fig. 11. Proposed closed-loop control for implementing MCSO.

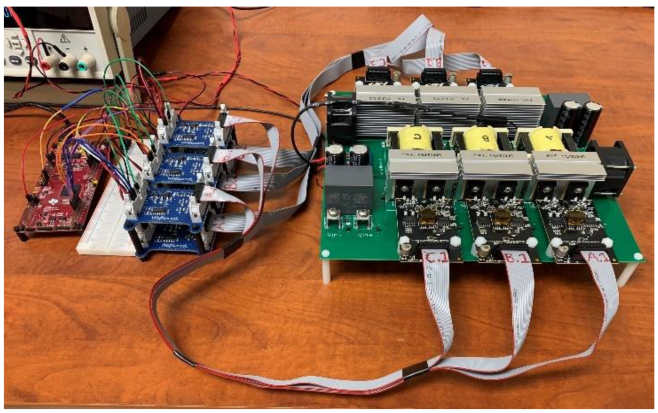

Fig. 12. 3p-DAB experimental prototype.

### G. Proposed Closed-Loop Control

Fig. 11 shows the proposed closed-loop control strategy for a 3p-DAB operating with the MCSO modulation scheme, which controls the output voltage $V_2$. Measurements of $V_1$, $V_2$, and $I_2$ facilitate the calculation of the output power $P_o$ and voltage gain $d$, which are fed into the MCSO block. Within the MCSO block, $P_o$ and $d$ are used with converter parameters to calculate the target mode of operation using the power boundaries given in (14), (17), (22), (26), and (28). Once the operating mode is selected, the MCSO block uses the closed-form DCC expressions [(13), (16), (21), (25), or (27)] to calculate target values $D_1*$, $D_2*$, and $D_{ps}*$ for optimal operation. Two slow-loop PI controllers are used to provide a gradual change between the calculated target duty cycle values and the generated duty cycle values $D_1$ and $D_2$. A slow loop is also used to gradually change $D_{ps}*$, which is added to the PI controller output for $V_2$ in order to meet the reference output voltage while compensating for the losses of the system. Furthermore, each control variable has saturation limits defined by the domain of the DCC (1).

## V. Experimental Results

A 1.125-kW 3p-DAB experimental prototype, shown in Fig. 12, was built and tested to validate the theoretical results. The proposed MCSO modulation scheme is experimentally compared to the traditional SPS modulation scheme [5], the proposed OMS using TDA (which is representative of the optimized modulation scheme given in [14], yet has the advantage of not requiring multifrequency approximation), and the ADCC scheme [16] (which is the only prior validated closed-form scheme proposed for the 3p-DAB with DCC). The converter specifications are listed in Table IV. During the experiments, the input bridge dc voltage $V_1$ was fixed to 150 V and the output bridge dc voltage $V_2$ varied depending on the desired voltage gain $d$. The input bridge dc-port was connected to a Sorenson SGX 600-25 power supply configured as a constant voltage source and the secondary bridge dc-port was connected to a Chroma 63800 electronic load configured in constant resistance mode.

TABLE IV
Parameters for 3p-DAB Prototype

| Parameter | Value |
|---|---|
| Rated power ($P_{\text{rated}}$) | 1125 W |
| Input dc voltage ($V_1$) | 150 V |
| Output dc voltage ($V_2$) | 90–195 V |
| Transformer turns ratio ($1{:}n$) | 1:1 |
| Switching frequency ($f_s$) | 20 kHz |
| Leakage inductance ($L_s$) | 83.33 $\mu$H |
| Input capacitance ($C_{in}$) | 275 $\mu$F |
| Output capacitance ($C_{\text{out}}$) | 275 $\mu$F |

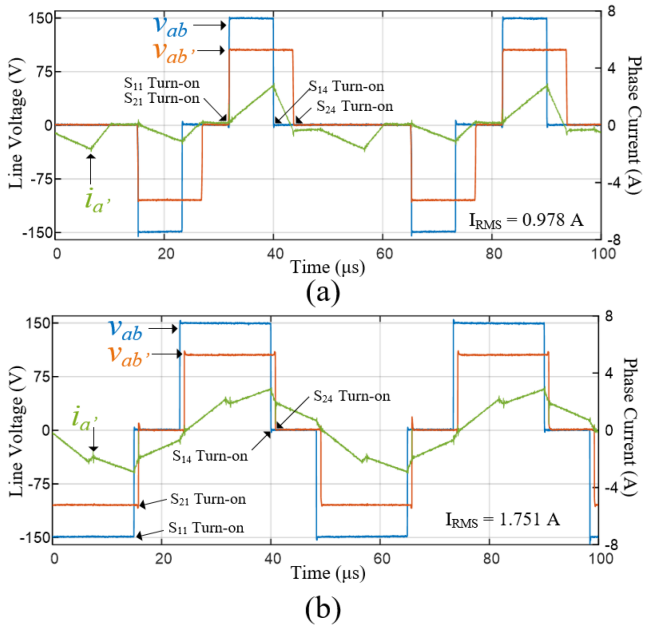


Fig. 13. Comparison of MCSO and SPS operating waveforms for low-power buck operation, $P_{\text{out}} = 0.1$ p.u. , $d = 0.7$. (a) Waveforms of MCSO in M2. (b) Waveforms of SPS.

Figs. 13 –16 present the operating waveforms of the proposed closed-form MCSO modulation scheme compared to the SPS modulation scheme at various operating points. To highlight the differences between the two modulation schemes, each experiment measured the primary and secondary line voltages ($v_{ab}$, $v'_{ab}$) and the output phase A transformer current ($i'_a$) over two switching periods at identical operating points ($P_{\text{out}}$, $d$). These waveforms capture the rms phase current and switch turn-ON events for both modulation schemes. If the body-diode of a particular switch is conducting at the turn-ON instant, ZVS will be achieved [5]. Similarly, if the switch current is zero at the turn-ON instant, ZCS will be achieved. Therefore, to determine

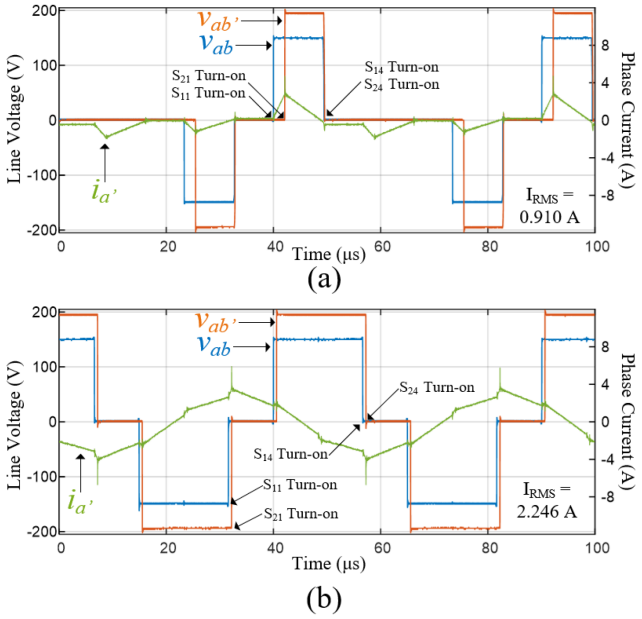


Fig. 14. Comparison of MCSO and SPS operating waveforms for low-power boost operation, $P_{\text{out}} = 0.1$ p.u., $d = 1.3$. (a) Waveforms of MCSO in M3. (b) Waveforms of SPS.

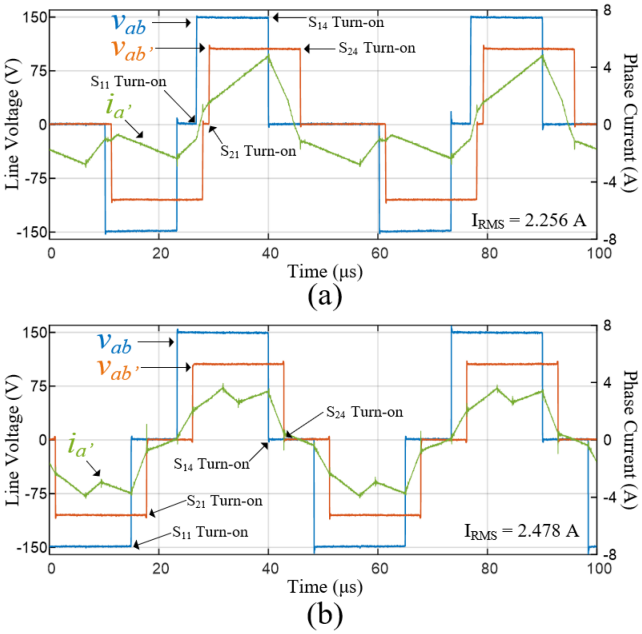


Fig. 15. Comparison of MCSO and SPS operating waveforms for medium-power buck operation, $P_{\text{out}} = 0.3$ p.u., $d = 0.7$. (a) Waveforms of MCSO in M15. (b) Waveforms of SPS.

whether a particular switch in a phase undergoes soft-switching at turn-ON, the polarity of the phase current can be analyzed at the turn-ON instant of that particular switch. Table V outlines the polarity requirements of the phase A current in order for a soft-switching event to occur in a phase A switch. The same requirements apply to phases B and C.

Fig. 13(a) presents the waveforms for low-power buck operation of the proposed MCSO modulation scheme and Fig. 13(b) shows the same for the SPS modulation scheme. In Fig. 13(a),

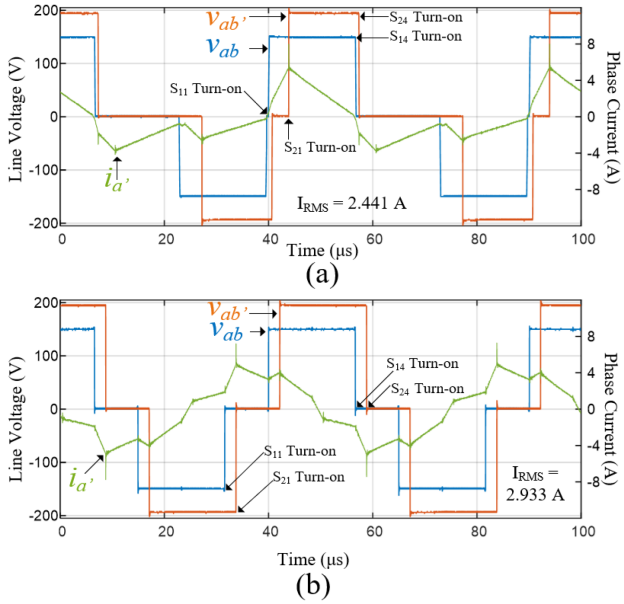


Fig. 16. Comparison of MCSO and SPS operating waveforms for medium-power boost operation, $P_{out} = 0.4$ p.u., $d = 1.3$. (a) Waveforms of MCSO in M10. (b) Waveforms of SPS.

TABLE V
PHASE A TURN-ON SOFT-SWITCHING REQUIREMENTS

| Switch | $I_{La} < 0$ | $I_{La} > 0$ | $I_{La} = 0$ |
|---|---|---|---|
| $S_{11}$ | ZVS | HSW | ZCS |
| $S_{14}$ | HSW | ZVS | ZCS |
| $S_{21}$ | HSW | ZVS | ZCS |
| $S_{24}$ | ZVS | HSW | ZCS |

the 3p-DAB operates in M2 of the MCSO thus the phase current is triangular. As a result, this modulation scheme enables soft-switching at turn-ON for all phase A switches ($S_{11}$, $S_{14}$, $S_{21}$, and $S_{24}$) and leads to a substantial reduction in rms phase current when compared to SPS. Fig 13(b) shows that when using SPS at the same operating point, the phase A output bridge switches $S_{21}$ and $S_{24}$ undergo HSW at turn-ON. Although these experimental waveforms are only for phase A, the balanced nature of this converter across all phases means that the respective switches in phases B and C undergo the same switching stresses as in phase A. Fig. 14 presents similar results for low-power boost operation (M3 in MCSO), the difference being that for SPS modulation shown in Fig. 14(b), the phase A input bridge switches $S_{11}$ and $S_{14}$ undergo HSW at turn-ON. Since the MCSO modulation scheme in the low-power range dramatically reduces the rms phase current and achieves ZCS/ZVS for all switches, the total losses are much lower than when operating with SPS, thereby improving the converter's efficiency in this region.

Similarly, Fig. 15(a) presents the waveforms for medium-power buck operation of the proposed MCSO modulation scheme, and Fig. 15(b) shows the same for the traditional SPS modulation scheme. In Fig. 15(a), the 3p-DAB operates with the MCSO scheme in M15. As a result, this modulation scheme enables ZVS at turn-ON for all phase A switches ($S_{11}$, $S_{14}$, $S_{21}$, and $S_{24}$) and leads to a small reduction in rms phase current

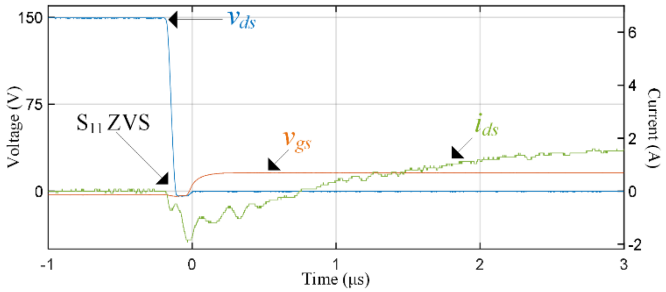


Fig. 17. ZVS switching waveforms for $S_{11}$ in M15 ($P_{\text{out}} = 0.3$ p.u., $d = 0.7$) showing ZVS at turn-ON.

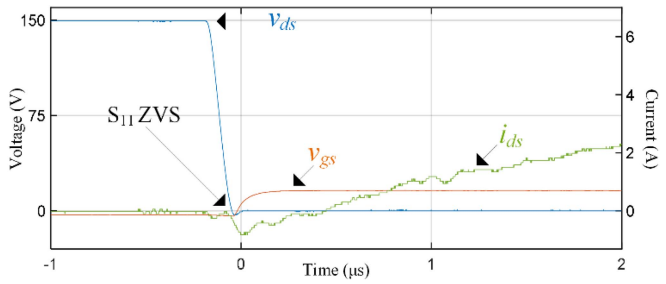


Fig. 18. ZVS switching waveforms for $S_{11}$ in M10 ($P_{\text{out}} = 0.4$ p.u., $d = 1.3$) showing ZVS at turn-ON.

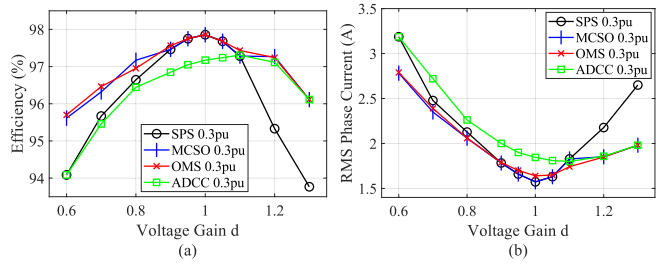


Fig. 19. Comparison of the SPS, proposed closed-form MCSO, OMS, and ADCC modulation schemes across wide voltage gain and fixed power level ($P_{\text{out}} = 337.5$ W). (a) Measured efficiency. (b) Transformer rms current.

when compared to SPS. Fig 15(b) shows that when using SPS at the same operating point, the phase A output bridge switches $S_{21}$ and $S_{24}$ undergo HSW at turn-ON. Fig. 16 presents similar results for medium-power boost operation (M10 in MCSO), the difference being that for SPS modulation shown in Fig. 16(b), the phase A input bridge switches $S_{11}$ and $S_{14}$ undergo HSW at turn-ON. Since the MCSO scheme in the medium-power range reduces the rms phase current and achieves ZVS for all switches, the total losses are lower than when operating with SPS, thereby improving the converter's efficiency in this region. To experimentally demonstrate the ZVS operation, Fig. 17 shows the ZVS turn-ON for $S_{11}$ operating in M15 ($P_{\text{out}} = 0.3$ p.u., $d = 0.7$) and Fig. 18 shows the ZVS turn-ON for $S_{11}$ operating in M10 ($P_{\text{out}} = 0.4$ p.u., $d = 1.3$). ZVS is achieved at turn-ON since the body diode of the MOSFET begins to conduct before the positive gate signal ($v_{gs}$) is applied.

The 3p-DAB efficiency and rms currents are measured over a wide range of output voltages and power levels to assess the performance of the proposed closed-form MCSO modulation scheme. Fig. 19(a) shows the measured efficiency of all four

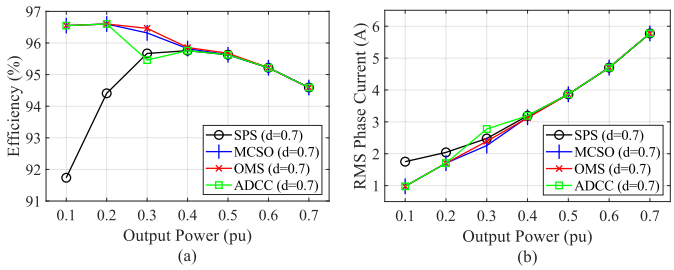


Fig. 20. Comparison of the SPS, proposed closed-form MCSO, OMS, and ADCC modulation schemes across large power range and fixed buck voltage gain ($d = 0.7$). (a) Measured efficiency. (b) Transformer rms current.

compared modulation schemes at a constant output power of 337.5 W (0.3 p.u.) with the output voltage varying from 90 V ($d = 0.6$) to 195 V ($d = 1.3$). Fig. 19(b) shows the rms current of the four modulation schemes over the same operating points. Fig. 19(a) shows that the efficiency of the 3p-DAB converter with SPS modulation decreasing as the voltage gain deviates from unity because of the increase in rms phase currents and loss of soft-switching operation. At this power level, the ADCC modulation scheme proposed in [16] operates in trapezoidal current mode and suffers from increased rms phase currents, even at voltage gains close to unity. The proposed MCSO scheme overcomes these drawbacks by minimizing the current stress and extending the soft-switching operating region of the 3p-DAB, thereby reducing both the switching and conduction losses at wide voltage gains. This results in an efficiency performance that very closely follows OMS and either matches or outperforms SPS and ADCC at all voltage gains. To quantify, the average of the efficiency points in Fig. 19(a) for OMS is 97.075% and the same average for MCSO is 97.052%. Thus, the efficiency of the closed-form MCSO is nearly identical to that of the OMS with offline optimization.

Fig. 20(a) and (b) present the efficiency and rms phase current measurements, respectively, for all four modulation schemes over a wide output power range and fixed buck voltage gain ($d = 0.7$). In the low-power region, OMS, ADCC, and MCSO efficiency curves match very closely and outperform the SPS modulation scheme. In the medium-power region the ADCC scheme operates using the trapezoidal current mode. Although operation in this mode achieves ZVS, the increased rms phase currents lead to a significant increase in conduction losses which negatively affect its efficiency. Lastly, in the high-power region, ADCC and MCSO adopt SPS modulation because of its ZVS and near optimal rms phase current operation. To quantify, the average of the efficiency points in Fig. 20(a) for OMS is 95.851% and the same average for MCSO is 95.818%. Again, the efficiency of the closed-form MCSO is nearly identical to that of the OMS.

Fig. 21(a) and (b) present similar measured efficiency and rms current, respectively, for a fixed boost voltage gain ($d = 1.3$). In the low-power region, ADCC, OMS, and the proposed MCSO modulation schemes all operate with triangular phase currents thus they achieve the same superior performance over SPS. In the medium-power region the ADCC control operates using the trapezoidal current mode. Although operation in this

TABLE VI
COMPARISON OF MULTIPLE DEGREE-OF-FREEDOM 3P-DAB MODULATION SCHEMES

| | Modulation Scheme | Objective of Modulation | ZVS Range[1] | RMS Current[2] | Number of Control Variables | Analyzed Voltage Gain Range ($d$) | Control Implementation | Comments |
|---|---|---|---|---|---|---|---|---|
| This work | MCSO | RMS current + current stress | wide | low | 3 | $0.5 < d < 1.5$ | closed-form | - Small hard-switching regions<br>- Buck and boost operation analyzed |
| [14] | OMS | RMS current | wide | low | 3 | $0 < d < 1$ | look-up table | - Offline optimization<br>- Multifrequency approximation<br>- Only buck operation analyzed |
| [12] | APS | RMS current | wide | low | 5 | $0 < d < 1$ | closed-form | - Unbalanced phase currents leading to increased component stresses and component oversizing<br>- Complex control<br>- Only buck operation analyzed |
| [11] | PPO | efficiency | wide | medium | 3 | $0.8 < d < 1.35$ | closed-form | - Unbalanced phase currents<br>- Operation as 1p-DAB increases dc-link ripple current |
| [15] | ZVM | efficiency | medium | low | 3 | $0.75 < d < 1.25$ | look-up table | - Offline optimization<br>- Requires detailed loss model |
| [16] | ADCC | ZVS | medium | medium | 3 | $0.5 < d < 1.5$ | closed-form | - Large hard-switching regions<br>- Increased RMS currents |
| [13] | SPWM | current stress | narrow | medium | 2 | $d > 0$ | closed-form | - SPS modulation for majority of operating range<br>- Minor efficiency improvement vs. SPS |

[1]Approximated based on area of HSW relative to full operating area on an operating plane ranging from zero to full power and analyzed voltage gain ($d$): *wide* ZVS range means < 8% of the operating area has HSW, *medium* ZVS range means 8%–30% of the operating area has HSW, and *narrow* ZVS range means > 30% of the operating area has HSW, where SPS has narrow ZVS range (for comparison).
[2]Based on modulation scheme's effect on rms phase current at low/medium powers relative to SPS: SPS is *high* (baseline), *low* achieves global or near-global minimum rms current, and *medium* has reduced rms current compared to SPS but does not achieve rms currents close to the global minimum.

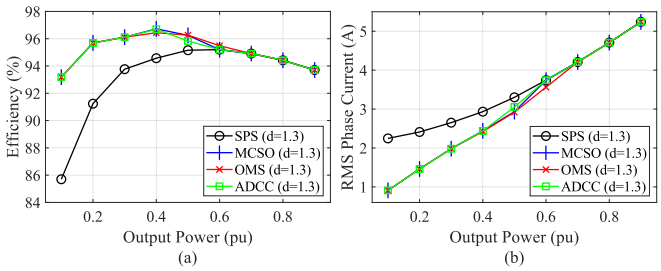


Fig. 21. Comparison of the SPS, proposed closed-form MCSO, OMS, and ADCC modulation schemes across large power range and fixed boost voltage gain ($d = 1.3$). (a) Measured efficiency. (b) Transformer rms current.

mode achieves ZVS, the increased rms phase currents lead to an increase in conduction losses which negatively affects its efficiency. In the high-power region, the ADCC and MCSO adopt SPS modulation because of its ZVS and near optimal rms phase current operation. To quantify, the average of the efficiency points in Fig. 21(a) for OMS is 95.135% and the same average for MCSO is 95.133%. The average efficiency of all points in Figs. 19(a), 20(a), and 21(a) is 96.020% for OMS and 96.001% for MCSO. Thus, the proposed closed-form MCSO modulation scheme is essentially equivalent to the offline-optimized OMS in terms of efficiency, with near-identical efficiency across the individual operating points.

Table VI summarizes and comments on the most recent 3p-DAB modulation schemes published in literature with two or more degrees of freedom in the control. The rows are ordered first by ZVS range and then by rms current, starting from the top. Control implementation is an important criterion as it impacts the practical feasibility of implementing a modulation scheme. LUT implementations require an offline optimization process to determine the optimal modulation parameters and can introduce interpolation errors. Furthermore, if a circuit parameter changes, the entire offline optimization process must be run again to generate a new LUT. Conversely, closed-form implementations, once derived, are much simpler to implement since the optimal modulation parameters can be calculated online in real time using the derived closed-form equations. The comparison in Table VI shows that compared to the other papers with wide ZVS range and low rms current ([14] and [12]), this work has closed-form solutions with only three control variables, does not have the disadvantage of unbalanced phase currents, and analyzes both buck and boost operation.

## VI. CONCLUSION

This article proposed a DCC modulation strategy for the 3p-DAB converter based on a comprehensive piecewise TDA and an optimization process that obtains the optimal control parameters for minimum rms phase current for buck and boost operation. Resulting from the TDA, 18 operating modes were defined by $D_1$, $D_2$, and $D_{ps}$. A nonlinear optimization problem was solved to obtain the optimal control parameters over a wide voltage and full power range. The results showed that only five of the 18 operating modes contributed to the optimized control, thus simplifying its implementation. Then, a novel closed-form DCC modulation scheme was proposed, MCSO, which was derived from the theoretical findings of the proposed TDA optimization method. The proposed MCSO scheme extends the soft-switching region and greatly reduces the rms phase currents during wide voltage and power variations thus improving the 3p-DAB's overall efficiency. The experimental results show that the proposed closed-form MCSO modulation scheme has equivalent efficiency to the OMS, making this the first article to provide a closed-form DCC modulation scheme for a 3p-DAB that achieves equivalent efficiency as a fully optimized offline

scheme, but without the drawbacks of the offline optimization process and LUT implementation.

## APPENDIX A

Appendix A provides the analytical expressions for average output power and rms phase current for the five optimal DCC modes M2, M3, M10, M15, and M16 that were not presented in the preceding sections of this article.

$$P_{\text{out}_{M10}} = P_{\text{out}_{M15}} \tag{A.1}$$

$$P_{out_{M16}} = P_{out_{M15}} \tag{A.2}$$

$$I_{\text{LRMS}_{M2}} = \frac{V_1 n}{3\sqrt{3}L_s f_s}\Big( -3d^2D_2^3 + 2d^2D_2^2 + 6dD_1^3 - 9dD_1^2D_2 - 18dD_1^2D_{ps} + 9dD_1D_2^2 + 18dD_1D_2D_{ps} - 4dD_1D_2 + 18dD_1D_{ps}^2 - 6dD_{ps}^3 - 3D_1^3 + 2D_1^2\Big)^{1/2} \tag{A.3}$$

$$I_{\text{LRMS}_{M3}} = \frac{V_1 n}{3\sqrt{3}L_s f_s}\Big( -3d^2D_2^3 + 2d^2D_2^2 + 9dD_1^2D_2 - 9dD_1D_2^2 - 18dD_1D_2D_{ps} - 4dD_1D_2 + 6dD_2^3 + 18dD_2^2D_{ps} + 18dD_2D_{ps}^2 - 3D_1^3 + 2D_1^2\Big)^{1/2} \tag{A.4}$$

$$I_{\text{LRMS}_{M10}} = \frac{-V_1 n}{9\sqrt{3}L_s f_s}\Big(27d^2D_2^3 - 18d^2D_2^2 - 54dD_1^3 + 81dD_1^2D_2 + 162dD_1^2D_{ps} - 81dD_1D_2^2 - 162dD_1D_2D_{ps} + 36dD_1D_2 - 162dD_1D_{ps}^2 + 27dD_2^3 + 81dD_2^2D_{ps} - 27dD_2^2 + 81dD_2D_{ps}^2 - 54dD_2D_{ps} + 9dD_2 + 81dD_{ps}^3 - 27dD_{ps}^2 + 9dD_{ps} - d + 9D_1^2 - 9D_1 + 1\Big)^{1/2} \tag{A.5}$$

$$I_{\text{LRMS}_{M16}} = \frac{-V_1 n}{9\sqrt{3}L_s f_s}\Big(9d^2D_2^2 - 9d^2D_2 + d^2 - 54dD_1^3 + 81dD_1^2D_2 + 162dD_1^2D_{ps} - 81dD_1D_2^2 - 162dD_1D_2D_{ps} + 36dD_1D_2 - 162dD_1D_{ps}^2 + 27dD_2^3 + 81dD_2^2D_{ps} - 27dD_2^2 + 81dD_2D_{ps}^2 - 54dD_2D_{ps} + 9dD_2 + 81dD_{ps}^3 - 27dD_{ps}^2 + 9dD_{ps} - d + 9D_1^2 - 9D_1 + 1\Big)^{1/2}. \tag{A.6}$$

## APPENDIX B

Appendix B provides the mathematical analysis of the turn-ON soft-switching conditions for all phase A switches of a 3p-DAB operating with the proposed MCSO modulation scheme. The analysis only needs to be conducted for the switches of a single phase because each phase operates with the same DCC parameters, just 120° phase-shifted from each other. For consistency, phase A is chosen, i.e., switches $S_{11}$, $S_{14}$, $S_{21}$, and $S_{24}$. Table VII summarizes the turn-ON instances of each phase A switch during a switching period and the phase current polarity requirement to achieve soft-switching. Therefore, the soft-switching conditions can be solved by checking to see if the polarity of the phase A current $i_a(t)$ at the turn-ON instant of each switch meets the requirements outlined in Table VII. The turn-ON soft-switching conditions are presented in Tables VIII–XI as inequality expressions of DCC parameters $D_1$, $D_2$, $D_{ps}$, and voltage gain $d$. The analysis confirms that all switches achieve turn-ON soft-switching for the proposed MCSO modulation scheme.

From Table XI, the requirement for $D_{ps}>(d-1)/3d$ can be deduced by realizing that in M3 and M10, $D_{ps}$ is a monotonically increasing function. In MCSO, M3 transitions into M10 as the output power increases. Since at the upper power boundary of M3, $D_{ps} = (d-1)/3d$, then in M10, $D_{ps}$ will always be greater than $(d-1)/3d$. Therefore, while operating in M10, $S_{11}$, $S_{14}$, $S_{21}$, and $S_{24}$ achieve ZVS.

TABLE VII
PHASE A TURN-ON SOFT-SWITCHING REQUIREMENTS

| Phase A Switch | Turn-on Instant | Soft-switching Requirement |
|---|---|---|
| $S_{11}$ – H.S. input bridge | $t = 0$ | $i_a(t) <= 0$ |
| $S_{14}$ – L.S. input bridge | $t = D_1$ | $i_a(t) >= 0$ |
| $S_{21}$ – H.S. output bridge | $t = D_{ps}$ | $i_a(t) >= 0$ |
| $S_{24}$ – L.S. output bridge | $t = D_2 + D_{ps}$ | $i_a(t) <= 0$ |

TABLE VIII
TURN-ON SOFT-SWITCHING CONDITIONS FOR M2

| Switch | Expression for Phase A Current at Switch Turn-on | Soft-switching Requirement from Table VII | Simplified Soft-switching Requirement | Statement |
|---|---|---|---|---|
| $S_{11}$ | $i_a(t) = \frac{nV_1}{3L_s f_s}(2t - D_1 + dD_2)$ | $i_a(t) \le 0$ $t = 0$ | $dD_2 - D_1 \le 0$ | ZCS for M2 since $D_1 = dD_2$ |
| $S_{14}$ | $i_a(t) = \frac{nV_1}{3L_s f_s}(D_1 - 2dt + dD_2 + 2dD_{ps})$ | $i_a(t) \ge 0$ $t = D_1$ | $d(D_2 - dD_2) \ge 0$ | ZVS for M2 since $d \le 1, D_2 > 0$ |
| $S_{21}$ | $i_a(t) = \frac{nV_1}{3L_s f_s}(2t - D_1 - 2dt + dD_2 + 2dD_{ps})$ | $i_a(t) \ge 0$ $t = D_{ps}$ | $dD_2 - D_1 \ge 0$ | ZCS for M2 since $D_1 = dD_2$ |
| $S_{24}$ | $i_a(t) = \frac{nV_1}{3L_s f_s}(D_1 - dD_2)$ | $i_a(t) \le 0$ $t = D_2 + D_{ps}$ | $dD_2 - D_1 \le 0$ | ZCS for M2 since $D_1 = dD_2$ |

TABLE IX
TURN-ON SOFT-SWITCHING CONDITIONS FOR M3

| Switch | Expression for Phase A Current at Switch Turn-on | Soft-switching Requirement from Table VII | Simplified Soft-switching Requirement | Statement |
|---|---|---|---|---|
| $S_{11}$ | $i_a(t) = \frac{nV_1}{3L_s f_s}(2t - D_1 + dD_2)$ | $i_a(t) \le 0$ $t = 0$ | $dD_2 - D_1 \le 0$ | ZCS for M3 since $D_1 = dD_2$ |
| $S_{14}$ | $i_a(t) = \frac{nV_1}{3L_s f_s}(D_1 - dD_2)$ | $i_a(t) \ge 0$ $t = D_1$ | $D_1 - dD_2 \ge 0$ | ZCS for M3 since $D_1 = dD_2$ |
| $S_{21}$ | $i_a(t) = \frac{nV_1}{3L_s f_s}(2t - D_1 - 2dt + dD_2 + 2dD_{ps})$ | $i_a(t) \ge 0$ $t = D_{ps}$ | $D_{ps} \ge 0$ | ZVS for M3 since $D_{ps} \ge 0$ |
| $S_{24}$ | $i_a(t) = \frac{nV_1}{3L_s f_s}(2t - D_1 - dD_2)$ | $i_a(t) \le 0$ $t = D_2 + D_{ps}$ | $D_2 \le \frac{D_{ps}}{(d-1)}$ | ZCS for M3 since $D_2 = \frac{D_{ps}}{(d-1)}$ |

TABLE X
TURN-ON SOFT-SWITCHING CONDITIONS FOR M15

| Switch | Expression for Phase A Current at Switch Turn-on | Soft-switching Requirement from Table VII | Simplified Soft-switching Requirement | Statement |
|---|---|---|---|---|
| $S_{11}$ | $i_a(t) = \frac{nV_1}{9L_s f_s}(6t + d - 3D_1 + 3dt - 3dD_{ps})$ | $i_a(t) \le 0$ $t = 0$ | $(1+d)D_{ps} \ge 0$ | ZVS for M15 since $d, D_{ps} > 0$ |
| $S_{14}$ | $i_a(t) = \frac{nV_1}{3L_s f_s}(D_1 - 2dt + dD_2 + 2dD_{ps})$ | $i_a(t) \ge 0$ $t = D_1$ | $D_{ps} + \frac{d}{3} + d^2D_{ps} \ge \frac{d^2}{3} + dD_{ps}$ | ZVS for M15 since $d \le 1, D_{ps} > 0$ |
| $S_{21}$ | $i_a(t) = \frac{nV_1}{9L_s f_s}(6t + d - 3D_1 - 3dt + 3dD_{ps})$ | $i_a(t) \ge 0$ $t = D_{ps}$ | $D_{ps} \ge 0$ | ZVS for M15 since $D_{ps} > 0$ |
| $S_{24}$ | $i_a(t) = \frac{nV_1}{9L_s f_s}(1 - 3t - d + 3D_1 + 3dt - 3dD_2 - 3dD_{ps})$ | $i_a(t) \le 0$ $t = D_2 + D_{ps}$ | $dD_{ps} \ge 0$ | ZVS for M15 since $d, D_{ps} > 0$ |

TABLE XI
TURN-ON SOFT-SWITCHING CONDITIONS FOR M10

| Switch | Expression for Phase A Current at Switch Turn-on | Soft-switching Requirement from Table VII | Simplified Soft-switching Requirement | Statement |
|---|---|---|---|---|
| $S_{11}$ | $i_a(t) = \frac{nV_1}{9L_s f_s}(3t - 1 + d + 3dt - 3dD_{ps})$ | $i_a(t) \le 0$ $t = 0$ | $D_{ps} \ge \frac{(d-1)}{3d}$ | *ZVS for M10 since $D_{ps} > \frac{(d-1)}{3d}$ |
| $S_{14}$ | $i_a(t) = \frac{nV_1}{9L_s f_s}(1 - 3t + 3D_1 - 6dt + 3dD_2 + 6dD_{ps})$ | $i_a(t) \ge 0$ $t = D_1$ | $D_{ps} \ge \frac{(d-1)}{3d}$ | *ZVS for M10 since $D_{ps} > \frac{(d-1)}{3d}$ |
| $S_{21}$ | $i_a(t) = \frac{nV_1}{3L_s f_s}(2t - D_1 - 2dt + dD_2 + 2dD_{ps})$ | $i_a(t) \ge 0$ $t = D_{ps}$ | $D_{ps} \ge \frac{(d-1)^2}{3(d^2-d+1)}$ | *ZVS for M10 since $D_{ps} > \frac{(d-1)}{3d}$ |
| $S_{24}$ | $i_a(t) = \frac{nV_1}{3L_s f_s}(1 - 3t + 3D_1 - 3dD_2)$ | $i_a(t) \le 0$ $t = D_2 + D_{ps}$ | $D_{ps} \ge \frac{(d-1)}{3d}$ | *ZVS for M10 since $D_{ps} > \frac{(d-1)}{3d}$ |

## REFERENCES


[1] B. Zhao, Q. Song, W. Liu, and Y. Sun, "Overview of dual-active-bridge isolated bidirectional DC–DC converter for high-frequency-link power-conversion system," *IEEE Trans. Power Electron.*, vol. 29, no. 8, pp. 4091–4106, Aug. 2014.

[2] M. A. H. Rafi and J. Bauman, "A comprehensive review of DC fast-charging stations with energy storage: Architectures, power converters, and analysis," *IEEE Trans. Transp. Electrific.*, vol. 7, no. 2, pp. 345–368, Jun. 2021.

[3] N. M. L. Tan, T. Abe, and H. Akagi, "Design and performance of a bidirectional isolated DC–DC converter for a battery energy storage system," *IEEE Trans. Power Electron.*, vol. 27, no. 3, pp. 1237–1248, Mar. 2012.

[4] A. Q. Huang, M. L. Crow, G. T. Heydt, J. P. Zheng, and S. J. Dale, "The future renewable electric energy delivery and management (FREEDM) system: The energy Internet," *Proc. IEEE*, vol. 99, no. 1, pp. 133–148, Jan. 2011.

[5] R. W. A. A. De Doncker, D. M. Divan, and M. H. Kheraluwala, "A three-phase soft-switched high-power-density DC/DC converter for high-power applications," *IEEE Trans. Ind. Appl.*, vol. 27, no. 1, pp. 63–73, Jan./Feb. 1991.

[6] M. N. Kheraluwala, R. W. Gascoigne, D. M. Divan, and E. D. Baumann, "Performance characterization of a high-power dual active bridge DC-to-DC converter," *IEEE Trans. Ind. Appl.*, vol. 28, no. 6, pp. 1294–1301, Nov./Dec. 1992.

[7] H. Bai and C. Mi, "Eliminate reactive power and increase system efficiency of isolated bidirectional dual-active-bridge DC–DC converters using novel dual-phase-shift control," *IEEE Trans. Power Electron.*, vol. 23, no. 6, pp. 2905–2914, Nov. 2008.

[8] B. Zhao, Q. Yu, and W. Sun, "Extended-phase-shift control of isolated bidirectional DC–DC converter for power distribution in microgrid," *IEEE Trans. Power Electron.*, vol. 27, no. 11, pp. 4667–4680, Nov. 2012.

[9] F. Krismer and J. W. Kolar, "Accurate small-signal model for the digital control of an automotive bidirectional dual active bridge," *IEEE Trans. Power Electron.*, vol. 24, no. 12, pp. 2756–2768, Dec. 2009.

[10] N. Hou and Y. W. Li, "Overview and comparison of modulation and control strategies for a nonresonant single-phase dual-active-bridge DC–DC converter," *IEEE Trans. Power Electron.*, vol. 35, no. 3, pp. 3148–3172, Mar. 2020.

[11] H. van Hoek, M. Neubert, and R. W. De Doncker, "Enhanced modulation strategy for a three-phase dual active bridge-boosting efficiency of an electric vehicle converter," *IEEE Trans. Power Electron.*, vol. 28, no. 12, pp. 5499–5507, Dec. 2013.

[12] H. Chen, S. Ouyang, J. Liu, and X. Li, "An Asymmetrical phase-shift scheme of three-phase dual active bridge with minimum current root-mean-square value control," *IEEE Trans. Power Electron.*, vol. 37, no. 12, pp. 14343–14361, Dec. 2022.

[13] J. Sun, L. Qiu, X. Liu, J. Zhang, J. Ma, and Y. Fang, "Optimal simultaneous PWM control for three- phase dual-active-bridge converters to minimize current stress in the whole load range," *IEEE J. Emerg. Sel. Topics Power Electron.*, vol. 9, no. 5, pp. 5822–5837, Oct. 2021.

[14] J. Huang, Z. Li, L. Shi, Y. Wang, and J. Zhu, "Optimized modulation and dynamic control of a three-phase dual active bridge converter with variable duty cycles," *IEEE Trans. Power Electron.*, vol. 34, no. 3, pp. 2856–2873, Mar. 2019.

[15] L. M. Cúnico, Z. M. Alves, and A. L. Kirsten, "Efficiency-optimized modulation scheme for three-phase dual-active-bridge DC–DC converter," *IEEE Trans. Ind. Electron.*, vol. 68, no. 7, pp. 5955–5965, Jul. 2021.

[16] J. Hu, Z. Yang, S. Cui, and R. W. De Doncker, "Closed-form asymmetrical duty-cycle control to extend the soft-switching range of three-phase dual-active-bridge converters," *IEEE Trans. Power Electron.*, vol. 36, no. 8, pp. 9609–9622, Aug. 2021.

[17] J. Sun, L. Qiu, X. Liu, J. Zhang, J. Ma, and Y. Fang, "Improved model predictive control for three-phase dual-active-bridge converters with a hybrid modulation," *IEEE Trans. Power Electron.*, vol. 37, no. 4, pp. 4050–4064, Apr. 2022.

[18] H. Jiao, R. Hao, Z. Lan, W. Zhu, S. Wang, and Z. Yan, "Research on three-degree-of-freedom control of three-phase dual active bridge to minimize current stress," in *Proc. IEEE 4th Int. Elect. Energy Conf.*, 2021, pp. 1–6.

[19] N. H. Baars, J. Everts, C. G. E. Wijnands, and E. A. Lomonova, "Modulation strategy for wide-range ZVS operation of a three-level three-phase dual active bridge DC-DC converter," in *Proc. IEEE Appl. Power Electron. Conf. Expo.*, 2017, pp. 3357–3364.

[20] R. U. Lenke, "A contribution to the design of isolated DC-DC converters for utility applications," Ph.D. dissertation, Inst. Power Gener. Storage Syst., E. ON Energy Res. Center, RWTH Aachen Univ., Aachen, Germany, 2012.

[21] A. Tong, L. Hang, G. Li, X. Jiang, and S. Gao, "Modeling and analysis of a dual-active-bridge-isolated bidirectional DC/DC converter to minimize RMS current with whole operating range," *IEEE Trans. Power Electron.*, vol. 33, no. 6, pp. 5302–5316, Jun. 2018.

[22] A. Rodríguez, A. Vázquez, D. G. Lamar, M. M. Hernando, and J. Sebastián, "Different purpose design strategies and techniques to improve the performance of a dual active bridge with phase-shift control," *IEEE Trans. Power Electron.*, vol. 30, no. 2, pp. 790–804, Feb. 2015.


**Gunnar Schulz** received the B.Eng. and M.A.Sc. degrees in electrical engineering from McMaster University, Hamilton, ON, Canada, in 2021 and 2023, respectively.

His research interests include design, control, and optimization of isolated bidirectional dual-active-bridge dc/dc converters for renewable and sustainable energy sources.

**Jennifer Bauman** (Senior Member, IEEE) received the B.Sc. and Ph.D. degrees in electrical engineering from the University of Waterloo, Waterloo, Canada, in 2004 and 2008, respectively.

From 2009 to 2016, she was the Director of Research with CrossChasm Technologies, Waterloo, ON, Canada, where she led the modeling team on a wide variety of automotive projects. She is currently an Associate Professor of Electrical Engineering with McMaster University, Hamilton, ON, Canada. Her research interests include power electronic converters for electrified powertrains, vehicle design, modeling, and control, and EV interactions with the smart grid.

Dr. Bauman is a registered Professional Engineer. She is currently an Associate Editor for IEEE OPEN JOURNAL OF POWER ELECTRONICS.